Title
Modeling heat transport processes in enhanced geothermal systems: A validation study from EGS Collab Experiment 1

Authors
Wu, Hui
Fu, Pengcheng
Frone, Zachary
et al.

Publication Date
2021-12-01

DOI
10.1016/j.geothermics.2021.102254

Peer reviewed

Published in *Geothermics*

Hui Wu, Pengcheng Fu, Zachary Frone, Mark D. White, Jonathan B. Ajo-Franklin, Joseph P. Morris, Hunter A. Knox, Paul C. Schwering, Christopher E. Strickland, Benjamin Q. Roberts, Vince R. Vermeul, Earl D. Mattson, Mathew D. Ingraham, Timothy J. Kneafsey, Douglas A. Blankenship, EGS Collab Team. (2021). Modeling heat transport processes in enhanced geothermal systems: A validation study from EGS Collab Experiment 1. Geothermics, 97, 102254.

Title: Modeling heat transport processes in enhanced geothermal systems: A validation study from EGS Collab Experiment 1

Author: Hui Wu[1], Pengcheng Fu[1], Zachary Frone[2], Mark D. White[3], Jonathan B. Ajo-Franklin[4], Joseph P. Morris[1], Hunter A. Knox[3], Paul C. Schwering[5], Christopher E. Strickland[3], Benjamin Q. Roberts[3], Vince R. Vermeul[3], Earl D. Mattson[6], Mathew D. Ingraham[5], Timothy J. Kneafsey[7], Douglas A. Blankenship[5], and the EGS Collab Team

Affiliation:

[1] Lawrence Livermore National Laboratory, Livermore, CA, USA.

[2] U.S. Department of Energy, Washington, DC, USA.

[3] Pacific Northwest National Laboratory, Richland, Washington, USA.

[4] Rice University, Texas, USA.

[5] Sandia National Laboratories, Albuquerque, New Mexico, USA.

[6] Mattson Hydrology, LLC, Victor, ID, USA.

[7] Lawrence Berkeley National Laboratory, Berkeley, CA, USA.

Corresponding author: Hui Wu (wu40@llnl.gov), Pengcheng Fu (fu4@llnl.gov)

Highlights:

- Analyzed heat transport processes in an intermediate-scale EGS field experiment.
- Developed a high-fidelity model incorporating a well-constrained fracture network.
- Demonstrated the capability in modeling heat recovery from EGS reservoirs

Abstract: Heat recovery from an enhanced geothermal system (EGS) is a complex process involving heat transport in both fracture networks and rock formations. A comprehensive understanding of and the ability to model the underlying heat transport mechanisms is important for the success of EGS commercialization but remains challenging in practice due to the generally insufficient characterization of EGS reservoirs. In the present study, we analyze an extensively monitored intermediate-scale EGS field experiment performed in a well-characterized testbed. The high-resolution, high-quality measurements from the field experiment enable the development of a high-fidelity model incorporating a well-constrained fracture network. Based on the field experiment, we investigate the complex heat transport processes in an EGS-relevant environment and validate the capability of a numerical approach in simulating these inherently coupled heat transport processes. A series of numerical simulations were performed to study the effects of different heat transport mechanisms, including thermal convection with fracture flow, thermal conduction in rock formations, and the Joule-Thomson effect. The agreement of thermal responses between field measurements and simulation results indicates that our numerical approach can appropriately model the heat transport processes pertaining to heat recovery from EGS reservoirs.

Keywords: Enhanced geothermal system, fracture network, heat transport, thermal convection, thermal conduction, Joule-Thomson effect.

---

1. Introduction

An enhanced geothermal system (EGS) extracts heat from hot dry rock (HDR) by creating subsurface fracture networks through which fluid can be circulated (Tester et al., 2006; Brown et al., 2012). The heat transport processes in EGS include thermal convection with fluid flow in fractures, thermal conduction in rock formations, and heat transfer between fracture fluid and rock formations (Gringarten et al., 1975; Bödvarsson and Tsang, 1982; Tester et al., 2006; Vik et al., 2018). These heat transport processes are inherently coupled. Direct observation of such heat transport processes is difficult, if not impossible, as HDR is normally located several kilometers below the ground surface. To understand the complex heat transport mechanisms, numerous laboratory experiments have been performed to investigate hydraulic conductivity of and heat transfer in fractured rocks (Luo et al., 2017; Chen and Zhao, 2020; Shu et al., 2020). Numerical models were developed to simulate heat transport processes in a thermo-hydro-mechanical (THM) coupled framework considering either a single fracture (Zeng et al., 2013; Guo et al., 2016; Asai et al., 2018; Patterson and Driesner, 2020) or a discrete fracture network (DFN) (Fu et al., 2016; Xia et al., 2017; Xu et al., 2018; Wang et al., 2019; Nadimi et al., 2020).

While important insights have been gained through laboratory experiments and numerical simulations, there still remains a strong necessity to obtain field observations and measurements for the following two purposes: 1) to test and improve our understanding of heat transport mechanisms in EGS, and 2) to validate numerical approaches for simulating coupled heat transport processes. Many EGS field projects, such as the Fenton Hill EGS in US and the Soultz-sous-Forêts EGS in France, invested tremendous effort in measuring mechanical, hydraulic, and thermal processes in response to field operations such as fracture stimulation, hydraulic characterization and continuous fluid circulation (Ayling et al., 2016;

Baria et al., 1999; Tenma et al., 2008; Brown et al., 2012). These real-world EGS reservoirs involve complex geological conditions, including, but not limited to, non-uniform temperature distribution, heterogeneous fracture aperture and *in situ* stress, and ubiquitous natural fractures. The spatially sparse field data were insufficient for characterizing these complex subsurface conditions, resulting in under-constrained reservoir models and limiting the utility of the field data for heat transport analysis and numerical model validation.

Intermediate-scale *in situ* experiments offer a complementary approach to investigating heat transport mechanisms in EGS reservoirs. Compared with full field-scale tests, an intermediate-scale experiment involves a relatively small testbed, allowing for finer resolution monitoring with a dense and diverse set of geophysical tools. High-quality, high-resolution field data can be obtained regarding mechanical, hydraulic and thermal processes in a realistic geological condition relevant to EGS reservoirs. Such a data-rich environment is particularly useful for comprehensively analyzing heat transport mechanisms pertaining to EGS reservoirs and validating numerical models for the simulation of heat recovery from EGS reservoirs.

The present study focuses on a long-term water circulation test conducted at the EGS Collab Experiment 1, an intermediate-scale EGS experiment, from March 2019 to February 2020. Based on the measured thermal responses, we propose three hypotheses regarding heat transport mechanisms to explain observed behavior of the testbed. We then use a THM modeling code to simulate the water circulation test with the purpose of testing the proposed hypotheses and validating the capability of our simulator in simulating coupled heat transport processes in EGS reservoirs. The remaining sections of this paper are organized as follows. Section 2 introduces the EGS Collab Experiment 1 testbed and a fracture network model developed from geological/geophysical observations and measurements. Section 3 first describes the long-term water circulation test, and then presents the observed thermal responses in monitoring and production wells. Three hypotheses regarding heat transport mechanisms are proposed to explain the thermal responses. In Section 4, we develop a 3D model to simulate the water circulation test and compare the simulation results with the measured temperature responses. Section 5 provides a discussion of the heat transport mechanisms and the utility of the intermediate-scale field test.

2. The EGS Collab Experiment 1 testbed

The EGS Collab project, sponsored by U.S. Department of Energy's Geothermal Technology Office, aims to bridge the gap between laboratory scale experiments and field scale EGS applications (White et al., 2019; Kneafsey et al., 2020). The project utilized a readily accessible underground facility to perform intermediate-scale field tests that are intensively monitored. Multiple experiments were planned to investigate different rock stimulation methods, including hydraulic fracturing (Experiment 1), shear stimulation (Experiment 2) and other potential stimulation methods (Experiment 3). Experiment 1 of the project started in 2017 and was completed in early 2020. The testbed of Experiment 1 is located in predominately phyllite rock of the Poorman formation, approximately 1478 m below ground surface, on the western side of the West Access Drift at the 4850 (nominal depth, in ft) Level within the Sanford Underground Research Facility (SURF) in Lead, South Dakota, USA. In what follows, we first introduce the design and geological conditions of the testbed, and then describe a fracture network model developed from field observations and measurements.

2.1 Geological conditions

The geological conditions of the testbed have been extensively described in previous studies, including *in-situ* stress (Dobson et al., 2017; White et al., 2018), natural fractures (Ulrich et al., 2018; Zhang et al., 2020; Fu et al., 2021; Wu et al., 2021), rock properties (Frash et al., 2019), etc., and are therefore not repeated here. Since the topic of the present study is thermal modeling and analysis, we focus on thermal conditions of the testbed.

Before becoming an underground research facility, SURF was the Homestake gold mine which was the largest and deepest gold mine in North America until its closure. The mining of the West Access Drift on the 4850 Level started in 1949. Mining, the abandonment of the mine, and the reopening of the facility for research have altered the state of the surrounding rock through ventilation, flooding, and dewatering. Consequently, the temperature profile surrounding the drift has changed significantly since 1949. White et al. (2018) summarized the sequence of major activities at the 4850 Level. To measure the temperature profile in the Experiment 1 testbed, several temperature surveys were conducted in 2009 and 2017 (Dobson and Salve, 2009; Oldenburg et al., 2017). A 2D numerical simulation considering the ambient geothermal gradient, hydrological state and major operations from 1949 to 2009 was performed to reconstruct the temperature, pore pressure and fluid saturation distributions around the West Access Drift (White et al., 2018). Both the temperature survey and the 2D simulation indicate a largely radial temperature gradient around the drift, resulting from the radial heat transport and fluid flow in the rock formations around the drift. The 2D simulation results provide an appropriate initial temperature distribution for the thermal modeling in the present study (Section 4).

2.2 Wellbore configuration

An injection well, a production well and six monitoring wells were drilled from the rib (wall) of the West Access Drift into the testbed (Fig. 1). All eight wells were nominally 60 meters long. The injection (E1-I) and production (E1-P) wells were approximately 10 m apart and were drilled nominally in the direction of the minimum horizontal principal stress (S_{hmin}) based on prior characterizations in the adjacent kISMET experiment (Oldenburg et al., 2017). The intention was to create hydraulic fractures perpendicular to E1-I and E1-P. Four monitoring wells (E1-PDT, E1-PDB, E1-PST and E1-PSB) were drilled parallel to the expected hydraulic fracture plane, and the other two monitoring wells (E1-OT and E1-OB) largely orthogonal to the expected hydraulic fracture. To provide sufficient monitoring of the hydraulic, mechanical, and thermal processes during stimulation and circulation tests, the six monitoring wells were comprehensively instrumented with various geophysical sensors including Continuous Active-Source Seismic Monitoring (CASSM), passive seismic monitoring (e.g. accelerometers and piezoelectric pressure transducers), electrical resistivity tomography (ERT) and distributed acoustic/temperature/strain sensing (DAS, DTS, DSS). A downhole camera was deployed in E1-P during some of the stimulation tests to directly observe fluid flow into the production well (Schwering et al., 2020).

We describe the DTS deployment due to its utilization in subsequent analysis. All fiber optic sensing measurements were conducted on a hybrid cable which included 4 single-mode and 4 multi-mode strands, tightly packed with aramid yarn and jacketed in polyethylene. The fiber optic cable was cemented into the six monitoring wells as a continuous loop with no splices to allow measurements from both directions at approximately 6800 locations. The cable was looped through two thermal baths in the drift before entrance and after exit from the monitoring wells, one kept at elevated temperature using a heated circulator (~40 °C) and a second at ambient drift temperature (~20 °C). Both baths were monitored using resistance temperature detectors to allow subsequent DTS calibration. DTS data were acquired continuously over the course of Experiment 1 with 10 minutes time averaging using a Raman-based interrogator unit (XT-DTS, Silixa LLC) sampling the fiber at 0.25 m spatial discretization. After acquisition, each independent data file was copied to a cloud repository where it was processed by an off-site server for real-time quality control and operational feedback. Absolute temperatures were obtained using the two-bath single-ended calibration scheme outlined by Hausner et al. (2011). The DTS sampling locations were spatially mapped to the well length by using the turn-around point and casing head as reference points to determine a stretch factor. The resulting profiles were then mapped to 3D using borehole deviation logs. We believe that the differential temperatures observed by DTS were accurate to below 0.1 °C while the absolute temperature values were slightly less accurate due to imperfect bath calibration.

2.3 Fracture network model

Multiple hydraulic stimulations were performed in the testbed in 2018 to create fractures that connect the injection and production wells. Subsequently, a series of flow and tracer tests were undertaken to characterize fracture trajectory and properties (White et al., 2019; Neupane et al., 2020). Fu et al. (2021) summarized the major hydraulic stimulation activities performed around 50 m depth in the injection well between May 22 and June 25, 2018. Based on field observations/measurements, Wu et al. (2021) developed a fracture network model consisting of a hydraulic fracture and a predominant natural fracture (called the “OT-P Connector”), as shown in Fig. 1.

The trajectory of the hydraulic fracture is delineated according to (1) microseismic events during hydraulic stimulations, (2) DTS signals along wells E1-OT and E1-PDT, and (3) fluid jetting in E1-P, as explained in Wu et al. (2021). The hydraulic fracture is roughly perpendicular to the S_{hmin} orientation. The propagation trajectory from 50 m depth in E1-I towards the West Access Drift is dictated by the decreasing S_{hmin} magnitude from E1-I to the drift caused by ventilation (e.g., cooling) in the drift. The OT-P Connector is a major natural fracture identified from televiewer logs and core samples (Fu et al., 2021; Wu et al., 2021).

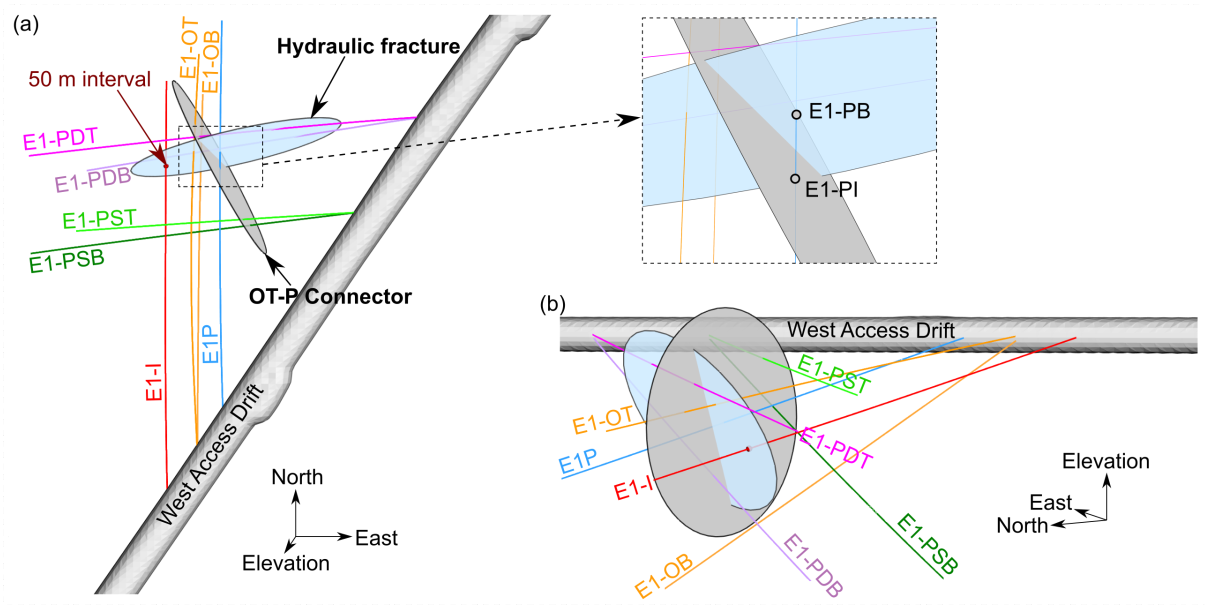

Fig. 1 The EGS Collab Experiment 1 testbed. (a) Plan view. (b) Side view. The injection well (E1-I), production well (E1-P), monitoring wells (E1-OT, E1-OB, E1-PST, E1-PSB, E1-PDT and E1-PDB) as well as the West Access Drift are shown. The 50 m-depth stimulation interval in the injection well is annotated. The fracture network model developed by Wu et al. (2021) is shown as the light blue and grey ellipses. The magnified inset shows the intersections of the production well with the hydraulic fracture and with the OT-P Connector, marked as E1-PB and E1-PI, respectively.

3. A long-term water circulation test

3.1 Water injection and outflow

After the establishment of hydraulic connectivity between the injection and production wells, a long-term water circulation test was conducted in the testbed from late March 2019 to early February 2020. Water, including chilled water when conditions permitted, was injected into the system between straddle packers at the 50 m-depth interval in the injection well (Fig. 1(a)). An injection rate of 400 ml/min was maintained for the majority of the water circulation test except for several interruptions mostly due to equipment or power issues. The initial injection temperature was maintained at approximately 28.0 °C, close to the temperature of the rock at the 50 m interval in the injection well. On May 8, 2019, chilled water circulation started with an injection temperature of approximately 12 °C. In several short periods, injection temperature was higher (e.g., ambient mine water temperature), mostly due to chiller failures.

Outflow was collected from multiple locations, and thermal responses were monitored at the production and monitoring wells. The total mass recovery ratio continuously increased and reached higher than 90% towards the end of the test (third panel in Fig. 2). Note that the main hydraulic fracture and the OT-P Connector intersected the production well (E1-P) at two depths, 39.5 m and 37.3 m, respectively. Flows into the production well from these two fractures were measured separately by setting a straddle packer centered at 37.3 m, thereby isolating the OT-P Connector flow in the packer "interval" and the hydraulic fracture flow below the packer assembly. Temperature and flow measurements from the "bottom" of the packer assembly were indicative of the hydraulic fracture's performance. In this paper, as well as in data released from the EGS Collab experiments, we use E1-PI and E1-PB to refer to these two intersections, with I and B denoting "interval" and "bottom", respectively. Fig. 1 shows the locations of these two intersections.

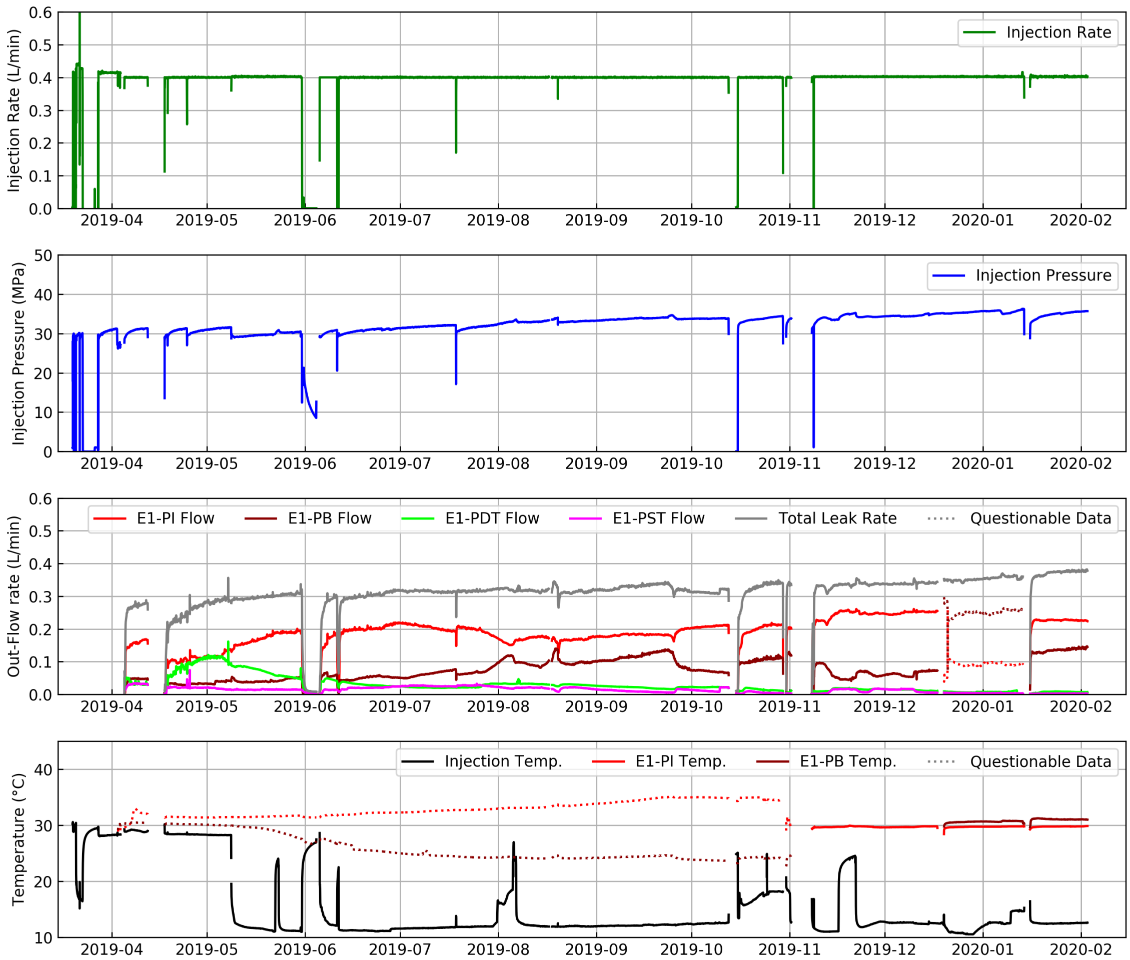

Fig. 2 Injection history of the long-term water circulation test performed at the EGS Collab Experiment 1 testbed. Injection rate and pressure are shown in the first and second panels respectively. Outflows were mainly observed at E1-P, E1-PDT and E1-PST as shown in the third row. The total outflow rate is also plotted. The fourth panel shows the injection and production temperatures. The dotted line segments in the third and fourth panels denote questionable outflow and temperature measurements as discussed in the text. Note that systematic and continuous measurements outflows started in early April 2019 as shown in the third panel.

3.2 Temperature responses at the production well

Two downhole unencapsulated thermistors were installed in the production well to monitor water temperatures at E1-PI and E1-PB respectively. The measured water temperature on April 3 was slightly higher at E1-PB (approximately 30.2 °C) than that at E1-PI (approximately 29.5 °C) as E1-PB was deeper in the production well than E1-PI (Fig. 3). After the interruption from April 4 to April 5, the temperatures at E1-PI displayed rather large changes, increasing to 33°C and then decreasing to 32°C on April 11. Largely continuous temperature measurements at these two locations were made between April 17 and November 11. During this period, measured temperature at E1-PB gradually decreased, which was interpreted to be thermal breakthrough, whereas measured E1-PI temperature gradually increased, which was speculated to reflect flow path evolution along the OT-P Connector. However, an inspection of the two thermistors in early November 2019 revealed that they might have been damaged (Kneafsey et al., 2020; White et al., 2020). A new thermistor with an improved design was installed at E1-PI in early November 2019 and a new thermistor for E1-PB was only available in mid-December 2019. Based on an analysis of the data, we concluded that temperature measurements at both locations were likely questionable between April 4 and the replacement of the thermistors, as indicated by the dotted line segments in Fig. 2. The measured temperatures at E1-PB and E1-PI after December 2019 were slightly higher than those measured on April 3, meaning that thermal breakthrough at the production well was not observed during the water circulation test.

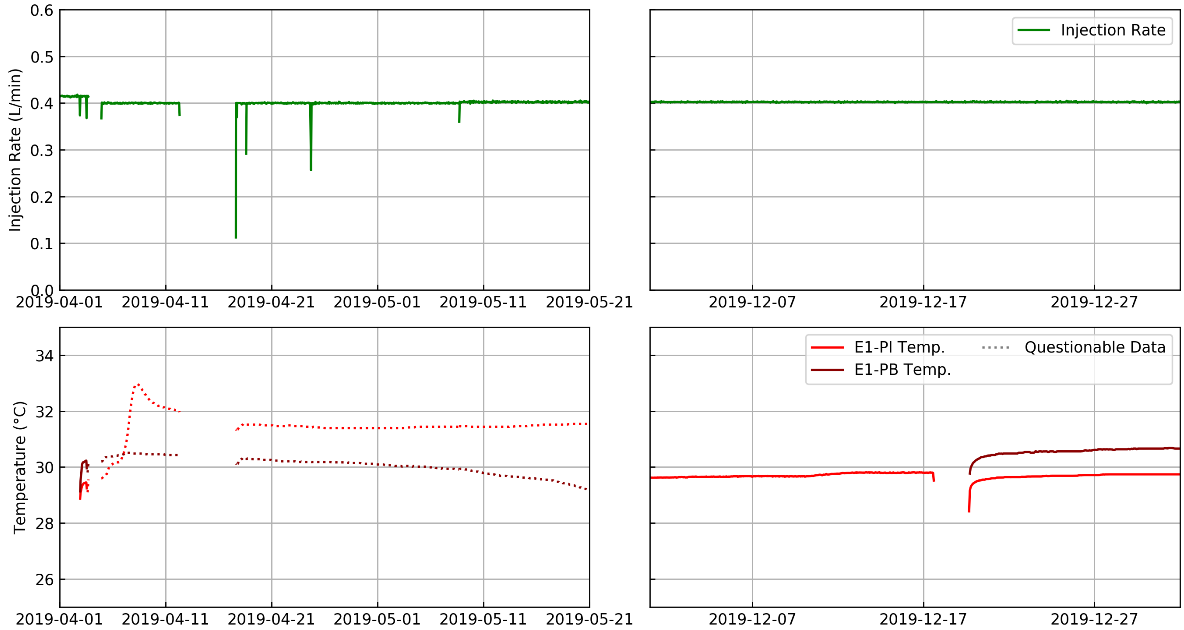

Fig. 3 Detailed view of E1-PI and E1-PB temperature measurements at the beginning of the measurement (left panels) when thermistor malfunction was likely to have started, and after the replacements of thermistors (right panels). The injection rate in these two periods is also shown.

3.3 Temperature profiles along the monitoring wells

Temperature profiles along the six monitoring wells were measured using DTS as described previously (Fig. 4(a)). In the baseline measurement, the increasing temperature from well collar to bottom is consistent with previous temperature surveys (Dobson and Salve, 2009; Oldenburg et al., 2017) and numerical simulations (White et al., 2018). With the injection of chilled water, the temperature in the six monitoring wells gradually changed. Major observations are summarized as follows:

- **Temperature increased at well collars**. According to the DTS measurements, temperatures at the collars of the six monitoring wells all increased from approximately 19.5 °C on 8 May to approximately 22.0 °C on 30 September (Fig. 4(b)), 2019. This can be attributed to the temperature increase in the West Access

Drift as a response to the seasonal temperature change at ground surface (via the ventilation system).

- **Temperature decreased at deep segments of the monitoring wells**. Despite the temperature increase near well collars, certain deep segments of the monitoring wells exhibited remarkable temperature decreases, presumably due to the circulation of chilled water. For E1-OT, E1-OB and E1-PDT, temperature decrease was observed for the majority of the well lengths. For E1-PSB, E1-PST and E1-PDB, temperature decrease was mainly observed for small segments of the wells, as manifested by the bowl-shaped temperature profiles at depths of approximately 31, 31 and 41 m in the three wells, respectively (Fig. 4(a)). A similar bowl-shaped temperature profile was also observed at approximately 40 m depth in E1-PDT.
- **Sharp temperature spikes were observed along E1-OT and E1-PDT**. The occurrence of sharp temperature spikes (Fig. 4(a)) appears to be related to the flow of water from fractures into E1-OT and E1-PDT. During the water circulation test, outflow was mainly monitored at E1-P, E1-OT, E1-PST and E1-PDT (Fig. 2), and sharp temperature spikes were observed at E1-OT and E1-PDT. In the late period of the circulation test, the outflow rates at E1-OT and E1-PDT gradually decreased to less than 5 mL/min, and the sharp temperature spikes became less significant correspondingly.

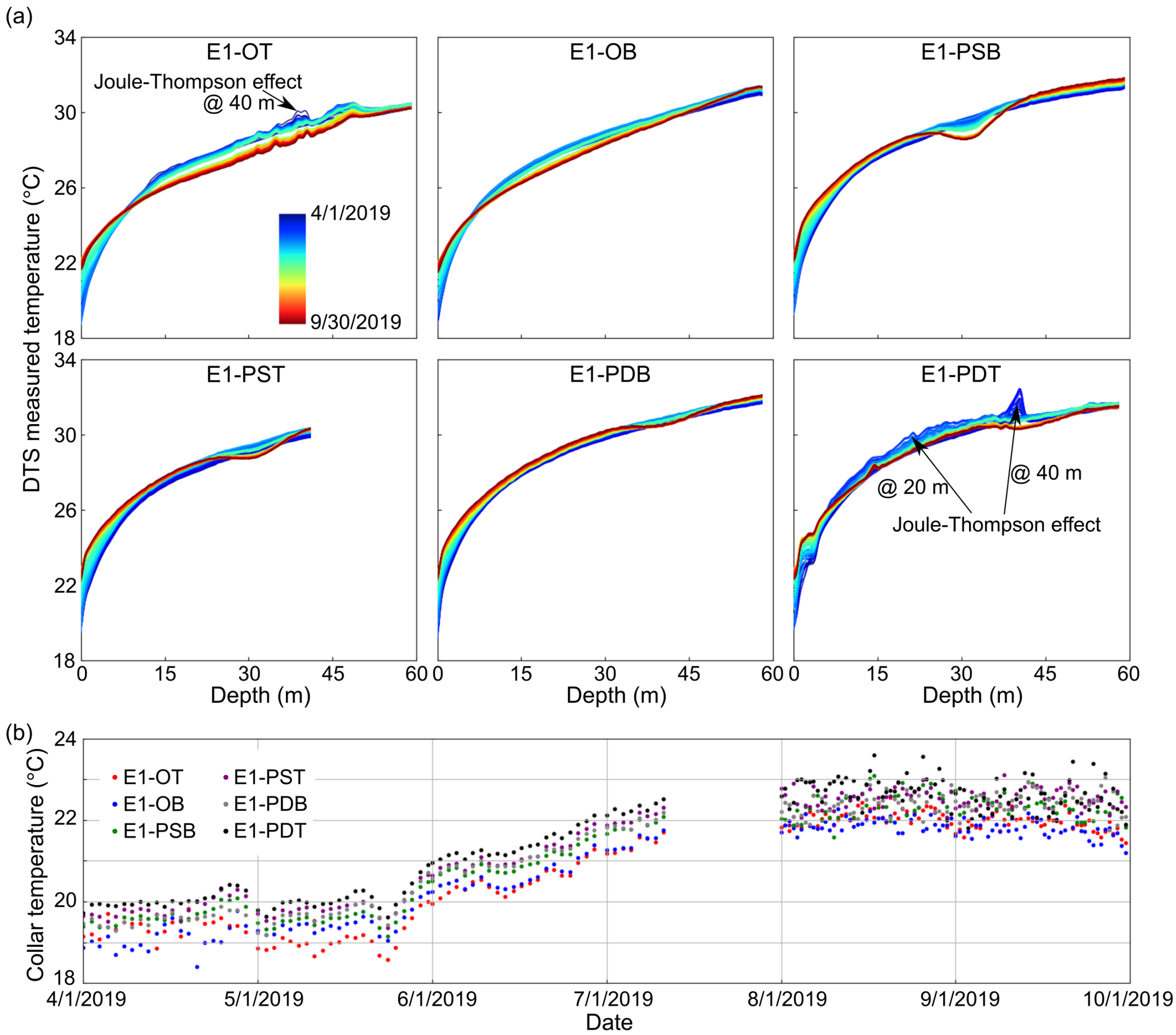

Fig. 4 Thermal responses in the monitoring wells. (a) Temperature profiles along the six monitoring wells from April 1 to September 30, 2019. (b) Collar temperature of the six monitoring wells. Note that data from July is unavailable due to equipment issues.

3.3 Hypotheses of heat transport mechanisms

Based on the thermal responses, we propose the following three hypotheses of heat transport mechanisms during the long-term water circulation test.

- **Temperature decrease in the monitoring wells was mainly caused by thermal conduction effect due to the cooling of the injection well**. The tubing carrying chilled water to the 50 m-depth interval in well E1-I was not adequately thermally insulated. Therefore, the segment between the collar and the injection interval, 50 m in total length, was subjected to cooling at approximately 12°C. This well segment then acted as a constant low temperature boundary in the testbed and affected the temperature distribution in the testbed through thermal conduction.

- **Thermal breakthrough at the production well was obscured by Joule-Thomson effect**. According to Fig. 2, water temperatures at E1-PB and E1-PI were approximately 30.2 and 29.5 °C respectively on April 1, 2019, and slightly increased to 30.5 and 30.0 °C respectively on December 31, 2019. Besides the aforementioned thermal convection and conduction effects, another important mechanism that affected outflow temperature in E1-P is the Joule-Thomson effect (Zhang et al., 2018; White and Fu, 2020). During the water circulation test, the injection pressure was approximately 30 - 36 MPa, while the pressure in E1-P was approximately atmospheric. The injected water might have encountered significant pressure drops when flowing from fractures into E1-P, as corroborated by the fluid jetting observed by downhole camera surveys (Schwering et al., 2020; Fu et al., 2021; Wu et al., 2021). The Joule-Thomson effect, as a result of near wellbore pressure drops and a negative Joule-Thomson coefficient, caused the increase of outflow temperatures at E1-PB and E1-PI, and obscured the thermal breakthrough behavior.
- **The sharp temperature spikes in E1-OT and E1-PDT were likely caused by the Joule-Thomson effect**. Similar to the outflow at E1-P, the outflow at E1-OT and E1-

PDT may also have experienced considerable pressure drops when flowing from the fracture network (Fig. 1) into wells. The corresponding Joule-Thomson effect manifested as the sharp spikes in the temperature profiles along E1-OT and E1-PDT. The Joule-Thomson effect can also explain the observation that the sharp spikes in E1-OT and E1-PDT became less significant with diminishing outflow rates in the late period of the water circulation test.

4. Modeling of the long-term water circulation test

To test the above hypotheses, we developed a 3D numerical model in GEOS, a multi-physics simulation environment developed at the Lawrence Livermore National Laboratory (Fu et al., 2013; Settgast et al., 2017). The formulations of the coupled THM modeling in GEOS are described in Guo et al. (2016) and not repeated here. Since the focus of the present study is to model the thermal processes associated with rock and fracture flow, we considered coupled hydro-thermal effects and ignored mechanical effect in the numerical model. We incorporate the temperature distribution simulated by White et al. (2018) and includes the fracture network model developed in Wu et al. (2021) (Fig. 5). By modeling the long-term water circulation test from March 28, 2019 to February 5, 2020, we also aim to validate the capability of GEOS in simulating complex heat transport processes in EGS reservoirs.

4.1 Model development

4.1.1 Model setup

Fig. 5 shows the domain of the 3D numerical model ($200 \times 200 \times 200$ m^3). The segment of E1-I between the collar and the 50 m interval is explicitly represented by a column of elements, each with a size of $0.1 \times 0.1 \times 0.1$ m^3, to appropriately simulate the cooling effect of E1-I during the water circulation test. The hydraulic fracture and the OT-P Connector are each represented by a 4 mm thick layer elliptical in shape (Fig. 5(b)). Considering the predominant role of the OT-P Connector (Wu et al., 2020), other natural fractures are not explicitly represented in the 3D model. Instead, we use a “pressure sink” on the periphery of the hydraulic fracture (Fig. 5) to account for water leakage from the hydraulic fracture to these natural fractures.

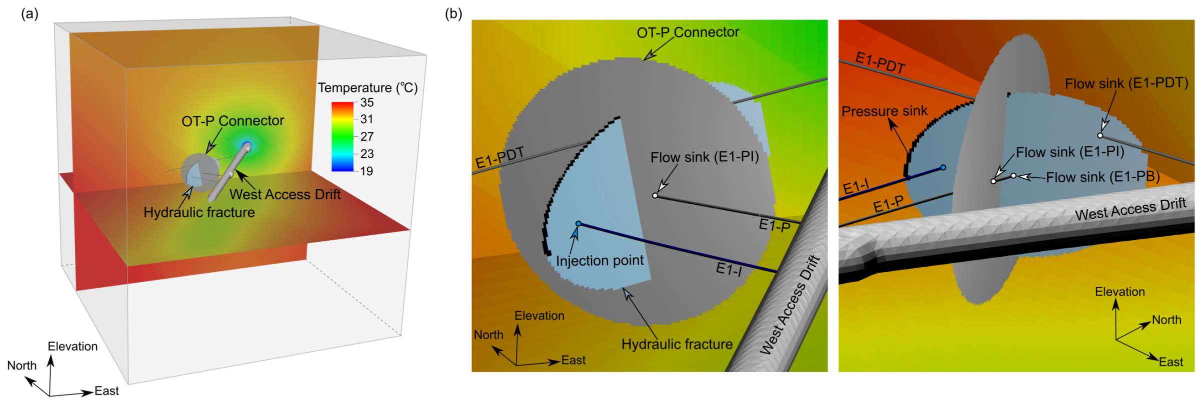

Fig. 5 The 3D numerical model for the simulation of the long-term water circulation test. (a) Initial temperature distribution in the model. The production well E1-P and monitoring well E1-PDT, as well as their intersections with the fractures are annotated. (b) Injection point, pressure sink (black elements on the periphery of the hydraulic fracture) and flow sinks in the numerical model.

Wu et al. (2020) inferred the location and length of the pressure sink, as well as the extents and aperture of the hydraulic fracture through stochastic modeling of a conservative tracer (C-Dots) test conducted on July 24, 2019. The results indicated that both uniform and heterogeneous aperture scenarios could reproduce the measured tracer data. Fig. 6 shows four satisfactory realizations of the hydraulic fracture’s effective aperture field that match the tracer data almost equally well, one with a uniform aperture and three with heterogeneous aperture distributions. The pressure sinks and the semi-axis lengths are also annotated. All four fracture realizations are considered in subsequent thermal modeling. For the OT-P Connector, the aperture distribution is assumed to be uniform with a value of 2 mm, which is directly estimated from natural fractures found in core samples. The two semi-axis lengths of the OT-P Connector are fixed at 20.0 m and 15.0 m.

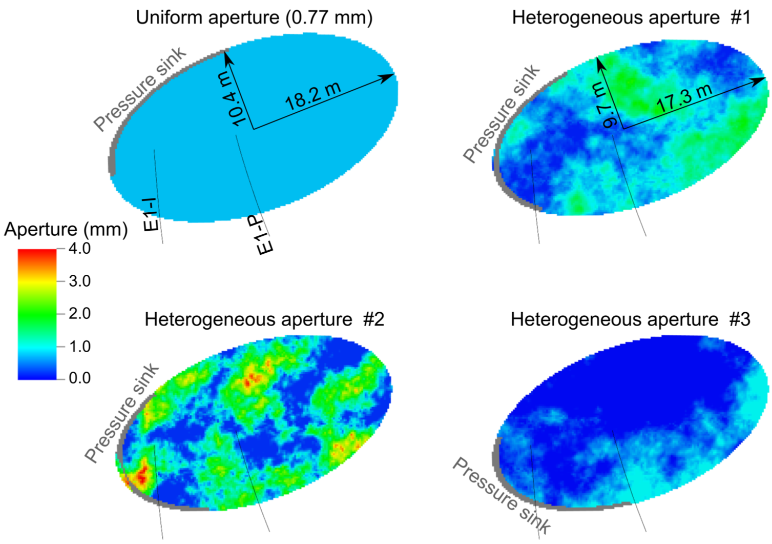

Fig. 6 Realizations of the hydraulic fracture shape and aperture field inferred from a conservative tracer test on July 24, 2019 (Wu et al., 2020). Note that the fracture extents are the same for the three heterogeneous aperture scenarios.

The mesh resolution is 0.2 m in the vicinity of E1-I and the two fractures, and gradually increases to 5 m in the far field. The in-plane resolution of the hydraulic fracture and the OT-P Connector is 0.2×0.2 m^2. The computational domain consists of 4,573,450 elements. Table 1 lists the parameters used for thermal modeling (Fu et al., 2018; White et al., 2018;).

Table 1: Rock and water parameters used for thermal modeling.

Parameter	Value
Porosity of rock	0.003

Solid density of rock (kg/m^3)	2500
Permeability of rock (m^2)	2×10^{-18}
Specific heat capacity of rock (J/kg/K)	790
Thermal conductivity of rock (W/m/K)	3.0
Water viscosity (Pa·s)	0.001
Specific heat capacity of water (J/kg/K)	4460
Water compressibility (Pa^{-1})	2×10^{-10}

4.1.2 Initial and boundary conditions

We extrapolate the 2D temperature distribution from White et al. (2018) to 3D by assuming that the temperature does not change along the drift axis direction. The 3D temperature distribution is then incorporated into the developed model as the initial temperature condition (Fig. 5(a)). To simulate the long-term water circulation test, temperatures at the upper, lower and lateral boundaries are held at the initial values. The temperature of the water injected into the fracture network is approximated from the measurements in Fig. 2 using a step function (Fig. 7(a)). The temperatures of the elements representing E1-I above the injection interval are fixed at the injection temperature, and the temperatures of the elements representing the drift are estimated from Fig. 4(b) to honor the seasonal temperature change in the drift.

A hydrostatic condition is assumed at the model boundaries. The injection rate is approximated from the measurements in Fig. 2 with a step function (Fig. 7(b)) and then applied to the injection point in Fig. 5(b). Note that the production and monitoring wells are not explicitly represented in the model. The outflows from E1-PB, E1-PI and E1-PDT (Fig. 2) are accounted for using “sinks” of specified outflow rates at fracture elements intersected by these wells (flow sinks in Fig. 5(b)). Similarly, we use step functions to approximate the outflow rates at these flow sinks (Fig. 7(c)). For the pressure sink, a constant pressure of 1 MPa is applied, which is equal to the hydrostatic pressure at the depth of the pressure sink.

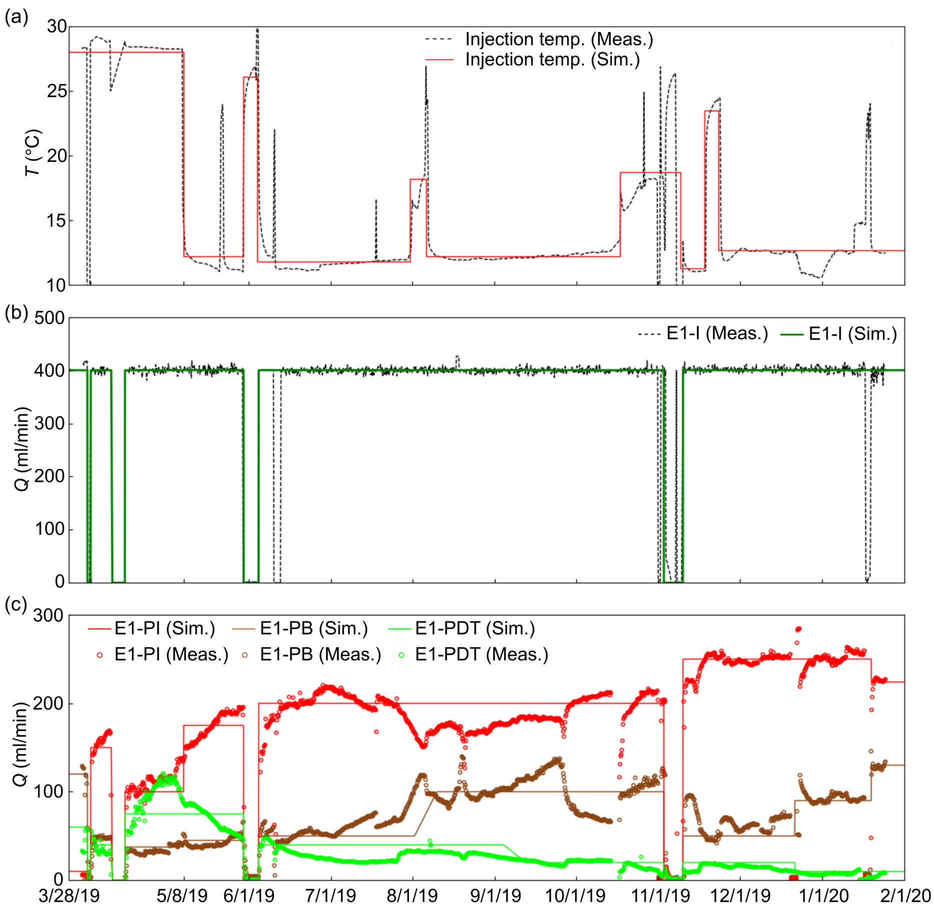

Fig. 7 Boundary conditions used in the numerical model. (a) Injection temperature. (b) Injection rate. (c) Outflow rates at E1-PB, E1-PI and E1-PDT.

4.2 Modeling of thermal responses in the monitoring wells

We first model the thermal responses in the six monitoring wells using the uniform aperture scenario in Fig. 6. Fig. 8 shows the temperature profiles along the six monitoring wells before and after chilled water injection, from both DTS measurements and thermal modeling. The observed temperature changes are appropriately reproduced, including the temperature decrease for the majority of E1-OT and E1-OB, as well as the bowl-shaped temperature profiles at specific depths in the other four monitoring wells. Fig. 9 compares the temperature distributions on three cross-sections on March 28 and September 30, 2019 to further demonstrate the heat transport processes during the water circulation test. Due to the cooling of E1-I, temperature decreases significantly along E1-I (Fig. 9(a)). Since E1-OT and E1-OB are almost parallel to E1-I, temperature also decreases along the majority of E1-OT and E1-OB through thermal conduction, as shown by the temperature profiles in Fig. 8. For the other four monitoring wells, the temperature decreases mainly occurred at well segments relatively close to E1-I (Fig. 9(b) and (c)). As a result, bowl-shaped temperature profiles were observed for E1-PDT, E1-PDB, E1-PST and E1-PSB in Fig. 8. Compared with E1-PDT and E1-PDB, E1-PST and E1-PSB (especially E1-PSB) are closer to the cooling segment of E1-I, and therefore the cooling of E1-I exerts larger impact on the temperature profiles in E1-PST and E1-PSB than that in E1-PDT and E1-PDB.

Both the cooling of E1-I and the chilled water circulation in the hydraulic fracture (HF) affected the temperature in the testbed. To test the first hypothesis in Section 3.3 that the temperature decrease in the monitoring wells is mainly caused by the cooling of E1-I, we performed two extra thermal simulations. One simulation only considers the cooling of E1-I, and the other simulation only considers the chilled water circulation in the hydraulic fracture. As shown in Fig. 10, due to the small injection rate (400 mL/min), the circulation of chilled water in the hydraulic fracture only affects the temperature near the injection point. For E1-OT, the temperature decrease along the segment between 5 and 40 m depths is mainly caused by E1-I cooling. For the segment between 40 and 50 m depths (note that the hydraulic fracture interested E1-OT at approximately 45 m depth), the temperature decrease caused by E1-I cooling is comparable to that caused by chilled water circulation in the hydraulic fracture (as shown in the zoomed-in plot for E1-OT in Fig. 11). Since E1-PSB and E1-PST are almost parallel to the hydraulic fracture and are relatively far from the hydraulic fracture, the bowl-shaped temperature profiles are mainly caused by E1-I cooling (Fig. 10(b)). As shown in the zoomed-in plot for E1-PSB and E1-PST in Fig. 11, the temperature change caused by chilled water circulation is very small (blue line), while E1-I cooling causes most of the temperature decrease (green dash line). E1-PDT and E1-PDB are relatively close to the hydraulic fracture, and the temperature decrease caused by chilled water circulation in the hydraulic fracture is comparable to that caused by E1-I cooling (Fig. 10(c) and Fig. 11).

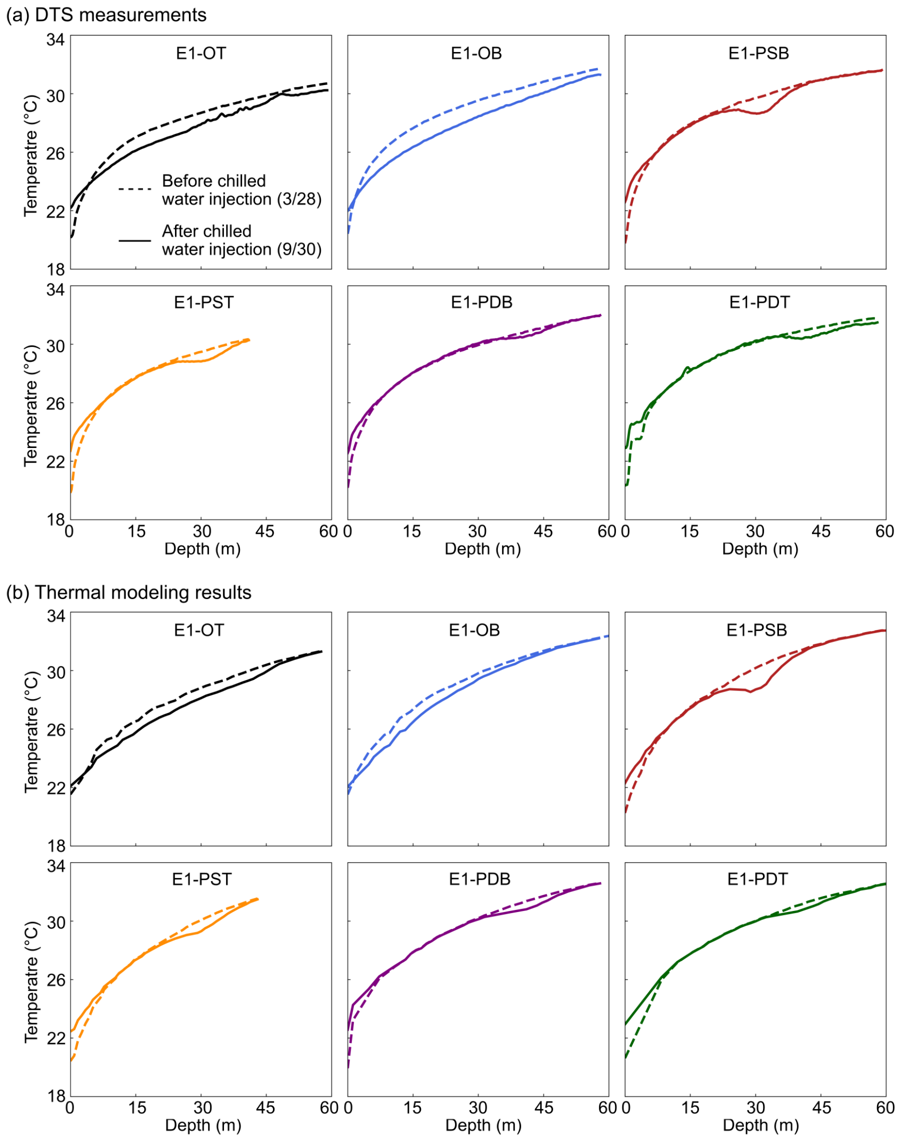

Fig. 8 Temperature profiles along six monitoring wells before and after chilled water injection from (a) DTS measurements and (b) Thermal modeling.

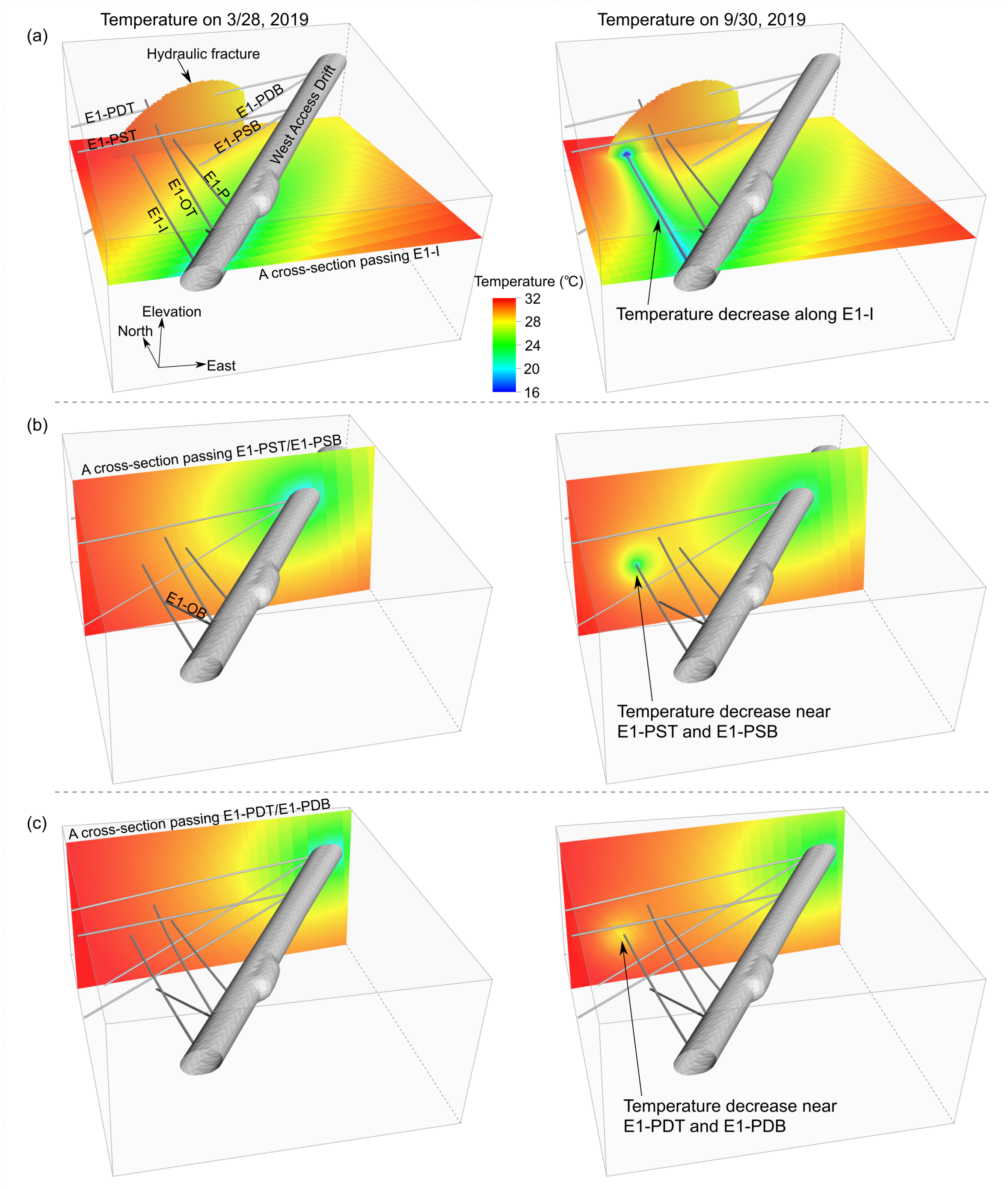

Fig. 9 Temperature distributions before and after chilled water injection. (a) Temperature on a cross-section passing E1-I. The hydraulic fracture is also shown. (b) Temperature on a cross-section passing E1-PST and E1-PSB. (c) Temperature on a cross-section passing E1-PDT and E1-PDB.

466 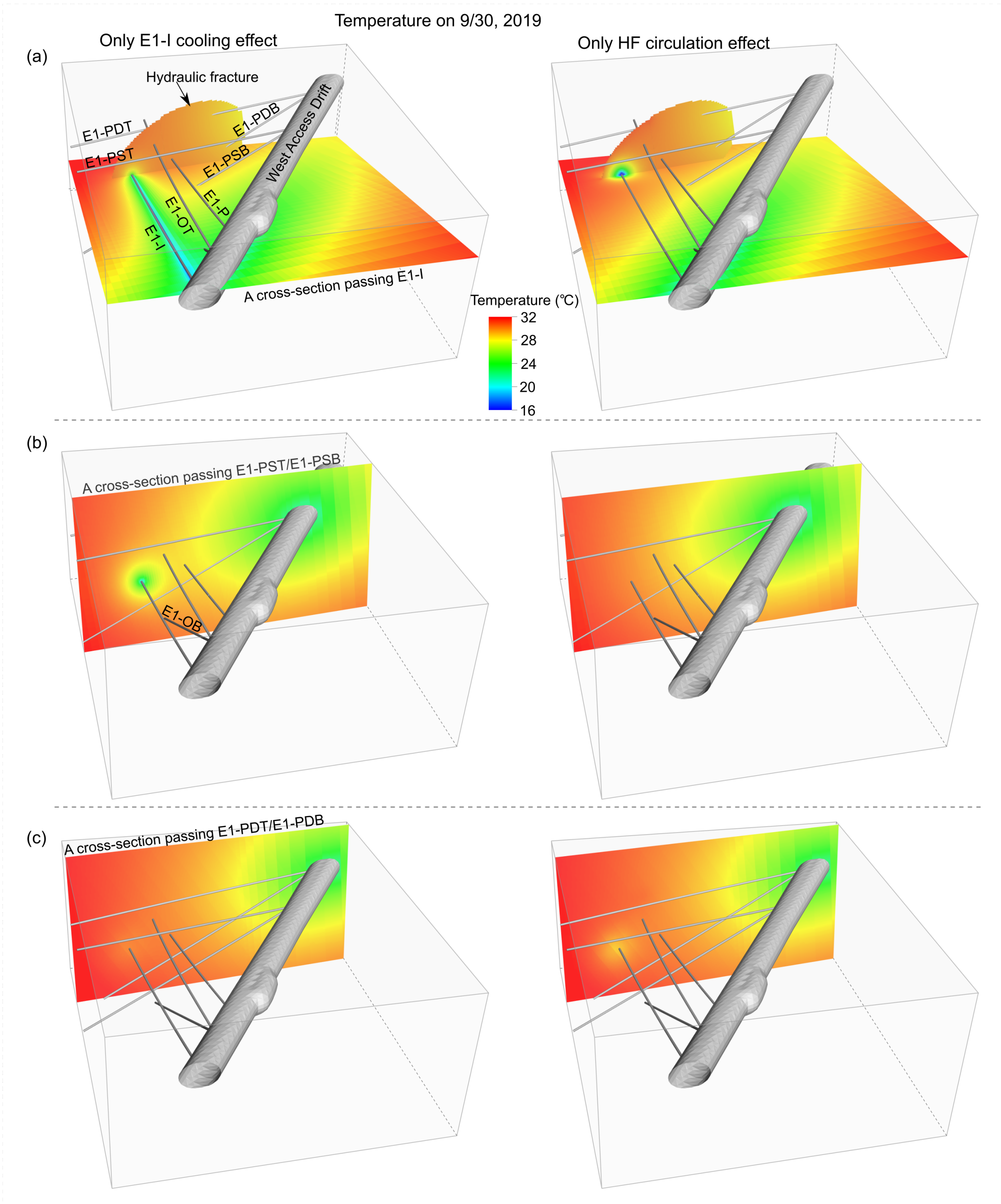

467 Fig. 10 Temperature change caused by E1-I cooling and chilled water circulation
468 respectively. (a) Temperature on a cross-section passing E1-I. (b) Temperature on a cross-
469 section passing E1-PST and E1-PSB. (c) Temperature on a cross-section passing E1-PDT and
470 E1-PDB.

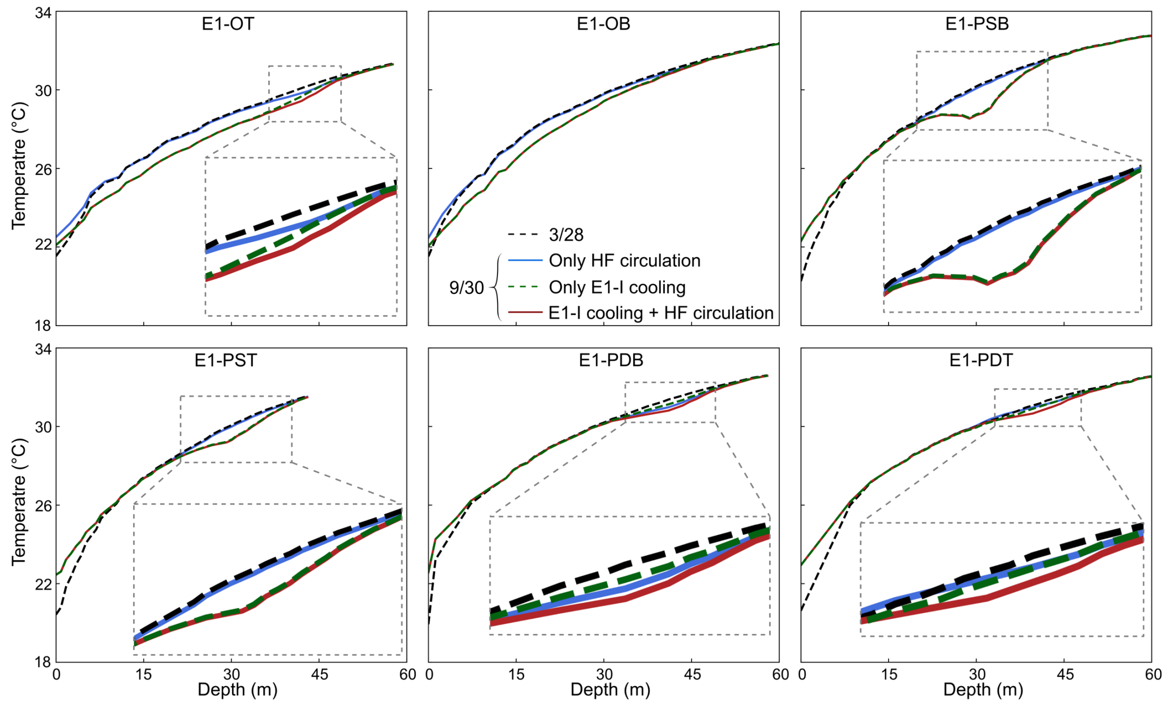

Fig. 11 Comparison of temperature changes in the six monitoring wells caused by E1-I cooling and chilled water circulation in the fracture network.

4.3 Modeling of thermal breakthrough at the production well

We consider both the uniform and heterogeneous aperture scenarios (Fig. 6) to simulate thermal breakthrough behavior at E1-PB and E1-PI (Fig. 12). In general, a heterogeneous aperture scenario induces faster thermal breakthrough than a uniform aperture scenario does due to relatively stronger flow channeling (Guo et al., 2016; Huang et al., 2019). However, for the fracture network in the present study, fracture flow depends on not only the aperture distribution but also the location of the pressure sink (Fig. 6). Compared with the pressure sink locations of the three heterogeneous aperture scenarios, the sink location of the uniform aperture scenario is closer to the production well. As a result, water flow from E1-I towards E1-P is accelerated, leading to faster temperature decreases at E1-PB and E1-PI (Fig. 12).

Although the four aperture scenarios can all reproduce the field conservative tracer data on July 24, 2019 (Wu et al., 2020), the predicted thermal breakthrough behavior is different and show considerable uncertainty (Fig. 12). Conservative tracer data alone is not sufficient to constrain the aperture distribution in the fracture model. To further reduce the uncertainty in the predicted thermal breakthrough behavior, other data such as sorptive tracer data should be used together with the conservative tracer data to invert for the aperture distribution.

Fig. 12 also shows the temperature response caused by E1-I cooling alone (the black dash line). For both E1-PB and E1-PI, the thermal conduction effect due to E1-I cooling is comparable to the thermal convection effect due to chilled water circulation in the hydraulic fracture. According to the modeling results in Fig. 12, in the end of the water circulation test, the temperature decreases by approximately 0.6 and 0.8 °C at E1-PB and E1-PI respectively, and the E1-I cooling effect alone induces approximately 0.4 °C temperature decrease at E1-PB and E1-PI.

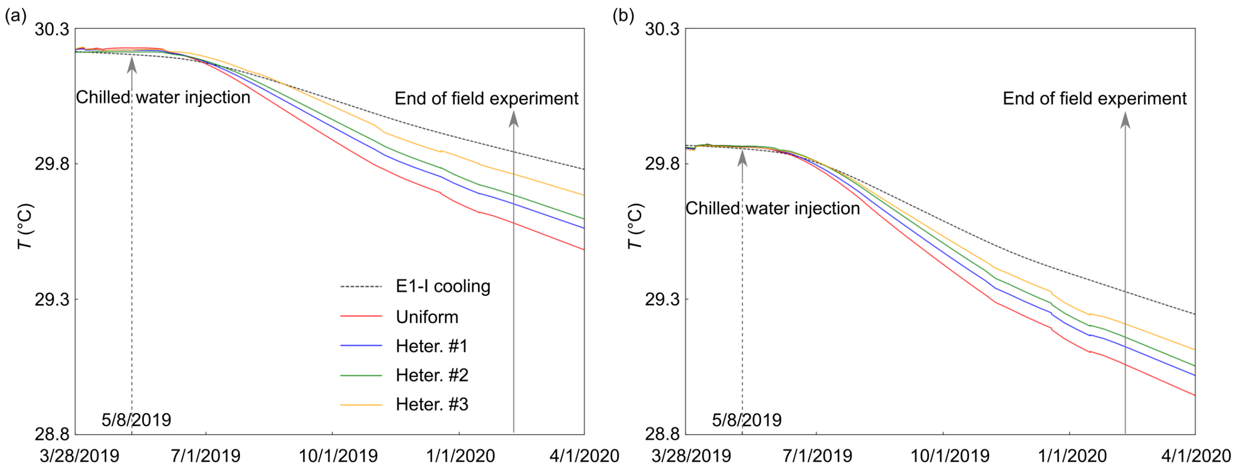

Fig. 12 Thermal breakthrough at the production well from numerical simulations. (a) Thermal breakthrough at E1-PB. The four aperture scenarios correspond to the results from stochastic tracer modeling in Fig. 6. The black dash line shows the results from the model that only considers E1-I cooling. (b) Thermal breakthrough at E1-PI.

However, according to the thermistor measurements in Fig. 3 (the solid lines), the temperature at E1-PB and E1-PI actually increased by approximately by 0.3 and 0.5 °C during the water circulation test. There are several factors affecting the outflow temperature at E1-PB and E1-PI: 1) Thermal convection with fracture flow tends to lower the outflow temperature and accelerates thermal breakthrough. 2) Heat exchange between fracture fluid and surrounding rocks, in contrast, warms the injected water and retards thermal breakthrough. 3) Thermal conduction due to E1-I cooling lowers the outflow temperature. 4) The Joule-Thomson effect causes temperature increase at E1-PB and E1-PI (White and Fu, 2020). The developed numerical model considers the first three factors but ignores the Joule-Thomson effect. The disagreement of the outflow temperatures at E1-PB and E1-PI between field measurements and simulation results is likely caused by the Joule-Thomson effect (the second hypothesis in Section 3.3).

We perform the following simple order-of-magnitude mathematical calculation to test the abovementioned hypothesis. Although we do not have a direct measurement of the temperature and pressure of water within the fracture before it jetted into well E1-P, reasonable assumptions are that (1) the pressure is higher than 20 MPa because the water needs to "jack" the fracture open, and (2) water temperature is approximately 30°C as it should be in an approximate equilibrium of the rock. The specific enthalpy of water at 20 MPa and 30 °C is 144 kJ/kg. After jetting into the wellbore, the pressure is close to the ambient atmospheric pressure. At a pressure of 0.1 MPa, water at 34.3°C would have a specific enthalpy of 144 kJ/kg. This means, without energy exchange with the surrounding rock, the water could have a 4.3°C temperature increase due to a sudden depressurization. Energy exchange is of course inevitable, but this value can serve as a rough upper-limit estimate of temperature increase due to the Joule-Thomson effect. The temperature change we need to reconcile the observations is well within this bound.

5. Discussion

5.1 Joule-Thomson effect caused temperature spikes in monitoring wells

Similar to the temperature increases at E1-PB and E1-PI (Fig. 2), the sharp temperature spikes along E1-OT and E1-PDT in Fig. 4 can also be explained by the Joule-Thomson effect (the third hypothesis in Section 3.3). The pressure drops when water flowed from the fracture network into E1-OT and E1-PDT cause sudden temperature increases. The temperature increases depend on the magnitude of the pressure drops, which could not be quantified, as well as the rate of heat dissipation through the surrounding rock. Note that although outflow was also monitored at E1-PST in the early stage of the water circulation test, we did not observe any temperature spike in the temperature profile along E1-PST (Fig. 4). A likely explanation is that the pressure drop when water flowed into E1-PST is too small to induce any remarkable temperature increase.

An important utility of the temperature spikes induced by the Joule-Thomson effect is the identification of intersections between fractures and wells. Note that there are two large temperature spikes in E1-PDT at the beginning of the water circulation test, one at 20 m depth and the other at 40 m depth (Fig. 4). The temperature spike at 20 m depth was first observed on October 30, 2018 during a hydraulic characterization test (Wu et al., 2021), and was interpreted as the intersection between the hydraulic fracture and E1-PDT (Wu et al., 2021). The temperature spike at 40 m depth was first observed on December 20, 2018 during another hydraulic stimulation at the 43 m interval in E1-I (Neupane et al., 2020), and was likely the result of the activation of a natural fracture intersecting E1-PDT at 40 m depth.

5.2 Utility of the intermediate-scale field experiment

Intermediate-scale field experiments provide a powerful approach to understanding mechanisms in complex processes/systems by achieving more realistic geologic conditions than core- or block-scale laboratory experiments, while allowing for better control and monitoring than full scale-field experiments. The intermediate-scale EGS Collab Experiment 1 involves realistic *in situ* stress conditions and natural fracture networks, enables performing hydraulic stimulation and water circulation tests in length- and time- scales relevant to field applications, and allows for intensive monitoring of these tests. The obtained field data provide a unique opportunity to understand the complex thermal, hydraulic and mechanical processes pertaining to heat recovery from EGS reservoirs. Borehole DTS measurements in particular provided strong constraints on thermal state through the course of the experiment, finely resolved in both space and time.

Meanwhile, we recognize that the differences in length, time and temperature scales between intermediate-scale experiments and full-size field applications deserve special attention to avoid misinterpretation of the thermal responses measured in intermediate-scale experiments. Our above analyses of the water circulation test reveal the significant roles of E1-I cooling and Joule-Thomson effect, which are mainly attributed to the relatively small experiment scales, including the short distance between the injection and production wells (approximately 10 m), relatively small injection rate (400 mL/min) and low temperature contrast between injected water and surrounding rocks (approximately 18 °C). In real-world EGS reservoirs, the distance between injection and production wells might be as large as 1 km, the injection rate as high as 100 L/s, and the temperature contrast as high as 160 °C (Tester et al., 2006). With the increase of well distance and injection rate, the impact of the cooling of injection well reduces rapidly, and fluid circulation in fracture network gradually dominates thermal breakthrough behavior. Additionally, the sharp pressure drops, thereby a strong Joule-Thomson effect, at the intersections between well E1-P and hydraulic fractures are unlikely to occur in a real EGS because the production well is subjected to back-pressure. Moreover, for an EGS reservoir with a temperature contrast of 160 °C and a life span of several decades, the Joule-Thomson effect-induced temperature change is negligible compared with the temperature change resulting from fluid circulation.

Nevertheless, this modeling exercise fulfills the objective of validating computer codes for EGS applications. Although certain processes play more significant roles in the intermediate-scale experiment than in a real EGS, the existence of and the interplay among the multiple heat transport mechanisms in this study enhances the "richness" of the dataset, thereby enabling a more comprehensive validation.

6. Conclusions

We presented a long-term water circulation test performed at an intermediate-scale testbed (EGS Collab Experiment 1) from March 2019 to February 2020. We developed a high-fidelity 3D numerical model with a fracture network inferred from geological/geophysical observations and measurements to simulate complex heat transport processes during the water circulation test. Field DTS measurements of temperature profiles in six monitoring wells were successfully reproduced. With measurement constrained fracture geometry and realistic representations of field conditions, the developed numerical model is capable of modeling key heat transport processes pertaining to heat recovery from EGS reservoirs, including thermal convection with fracture flow and thermal conduction in rock formations.

For the intermediate-scale EGS Collab Experiment 1, the Joule-Thomson effect, resulting from abrupt pressure drops when fluid flows from fractures into wellbores and manifesting as sudden temperature increases, shows considerable impact on observed thermal responses in the testbed. First, the temperature spikes monitored by DTS are useful in identifying intersections between fractures and wellbores, and thus provide reliable information for the delineation of fracture trajectory. Second, the temperature increase induced by the Joule-Thompson effect slows down thermal breakthrough at the production well.

Acknowledgments

This research was performed in support of the EGS Collab project; taking place in part at the Sanford Underground Research Facility in Lead, South Dakota. The assistance of the Sanford Underground Research Facility and its personnel in providing physical access and general logistical and technical support is acknowledged. Support from the EGS Collab team is gratefully acknowledged. This work was supported by U.S. Department of Energy, Geothermal Technologies Office, and performed under the auspices of the U.S. Department of Energy by Lawrence Livermore National Laboratory under Contract DE-AC52-07NA27344. Sandia National Laboratories is a multimission laboratory managed and operated by National Technology & Engineering Solutions of Sandia, LLC, a wholly owned subsidiary of Honeywell International Inc., for the U.S. Department of Energy's National Nuclear Security Administration under contract DE-NA0003525. This paper describes objective technical results and analysis. Any subjective views or opinions that might be expressed in the paper do not necessarily represent the views of the U.S. Department of Energy or the United States Government. This document is LLNL report LLNL-JRNL-821457.

The EGS Collab Team includes J. Ajo-Franklin, T. Baumgartner, K. Beckers, D. Blankenship, A. Bonneville, L. Boyd, S. Brown, J.A. Burghardt, C. Chai, A. Chakravarty, T. Chen, Y. Chen, B. Chi, K. Condon, P.J. Cook, D. Crandall, P.F. Dobson, T., C.A. Doughty, D. Elsworth, J. Feldman, Z. Feng, A. Foris, L.P. Frash, Z. Frone, P. Fu, K. Gao, A. Ghassemi, Y. Guglielmi, B. Haimson, A. Hawkins, J. Heise, C. Hopp, M. Horn, R.N. Horne, J. Horner, M. Hu, H. Huang, L. Huang, K.J. Im, M. Ingraham, E. Jafarov, R.S. Jayne, T.C. Johnson, S.E. Johnson, B. Johnston, S. Karra, K. Kim, D.K. King, T. Kneafsey, H. Knox, J. Knox, D. Kumar, K. Kutun, M. Lee, D. Li, J. Li, K. Li, Z. Li, M. Maceira, P. Mackey, N. Makedonska, C.J. Marone, E. Mattson, M.W. McClure, J. McLennan, T. McLing, C. Medler, R.J. Mellors, E. Metcalfe, J. Miskimins, J. Moore, C.E. Morency, J.P. Morris, T. Myers, S. Nakagawa, G. Neupane, G. Newman, A. Nieto, T. Paronish, R. Pawar, P. Petrov, B. Pietzyk, R.

Podgorney, Y. Polsky, J. Pope, S. Porse, J.C. Primo, C. Reimers, B.Q. Roberts, M. Robertson, V. Rodriguez-Tribaldos, W. Roggenthen, J. Rutqvist, D. Rynders, M. Schoenball, P. Schwering, V. Sesetty, C.S. Sherm, A. Singh, M.M. Smith, H. Sone, E.L. Sonnenthal, F.A. Soom, D.P. Sprinkle, S. Sprinkle, C.E. Strickland, J. Su, D. Templeton, J.N. Thomle, C. Ulrich, N. Uzunlar, A. Vachaparampil, C.A. Valladao, W. Vandermeer, G. Vandine, D. Vardiman, V.R. Vermeul, J.L. Wagoner, H.F. Wang, J. Weers, N. Welch, J. White, M.D. White, P. Winterfeld, T. Wood, S. Workman, H. Wu, Y.S. Wu, E.C. Yildirim, Y. Zhang, Y.Q. Zhang, Q. Zhou, M.D. Zoback.

References

Asai, P., Panja, P., McLennan, J., Moore, J., 2018. Performance evaluation of enhanced geothermal system (EGS): Surrogate models, sensitivity study and ranking key parameters. Renewable Energy 122, 184-195.

Ayling, B.F., Hogarth, R.A., Rose, P.E., 2016. Tracer testing at the Habanero EGS site, central Australia. Geothermics 63, 15-26.

Baria, R., Baumgärtner, J., Gérard, A., Jung, R., Garnish, J., 1999. European HDR research programme at Soultz-sous-Forets (France) 1987-1996. Geothermics 28, 655-669.

Bödvarsson G.S., Tsang, C.F., 1982. Injection and Thermal Breakthrough in Fractured Geothermal Reservoirs. Journal of Geophysical Research: Solid Earth 87, 1031-1048.

Brown, D.W., Duchane, D.V., Heiken, G., Hriscu, V.T., 2012. Mining the Earth's Heat: Hot Dry Rock Geothermal Energy. Springer, Berlin.

Chen, Y., Zhao, Z., 2020. Heat transfer in a 3D rough rock fracture with heterogeneous apertures. International Journal of Rock Mechanics and Mining Sciences 134, 104445.

Dobson, P.F., R. Salve., 2009. Underground reconnaissance and environmental monitoring related to geologic CO_2 sequestration studies at the DUSEL facility, Homestake Mine, South Dakota. LBNL-2858E, Lawrence Berkeley National Laboratory, Berkeley, CA.

Dobson, P.F., Kneafsey, T.J., Blankenship, D., Valladao, C., Morris, J.P., Knox, H., et al., 2017. An introduction to the EGS Collab Project. GRC Transactions 41, 837-849.

Frash, L.P., Carey, J.W., Welch, N.J., EGS Collab Team, 2019. EGS Collab Experiment 1 geomechanical and hydrological properties by triaxial direct shear. 44th Workshop on Geothermal Reservoir Engineering, Stanford University, Stanford, CA.

Fu, P., Hao, Y., Walsh, S.D.C., Carrigan, C.R., 2016. Thermal drawdown-induced flow channeling in fractured geothermal reservoirs. Rock Mechanics and Rock Engineering 49, 1001-1024.

Fu, P., Johnson, S.M., Carrigan, C.R., 2013. An explicitly coupled hydro-geomechanical model for simulating hydraulic fracturing in arbitrary discrete fracture networks. International Journal for Numerical and Analytical Methods in Geomechanics 37, 2278-2300.

Fu, P., Schoenball, M., Ajo-Franklin, J.B., Chai, C., Maceira, M., Morris, J.P. et al., 2021. Close observation of hydraulic fracturing at EGS Collab Experiment 1: Fracture trajectory, microseismic interpretations, and the role of natural fractures. Journal of Geophysical Research: Solid Earth 126, e2020JB020840.

Fu, P., White, M.D., Morris, J.P., Kneafsey, T.J., EGS Collab Team., 2018. Predicting hydraulic fracture trajectory under the influence of a mine drift in EGS Collab Experiment 1. 43rd Workshop on Geothermal Reservoir Engineering, Stanford University, Stanford, CA.

Gringarten, A.C., Witherspoon, P.A., Ohnishi, Y., 1975. Theory of heat extraction from fractured hot dry rock. Journal of Geophysical Research 80(8), 1120-1124.

Guo, B., Fu, P., Hao, Y., Peters, C.A., Carrigan, C.R., 2016. Thermal drawdown-induced flow channeling in a single fracture in EGS. Geothermics 61, 46-62.

Hausner, M.B., Suarez, F., Glander, K.E., van der Giesen, N., Selker, J.S., Tyler, S.W., 2011. Calibrating single-ended fiber-optic raman spectra distributed temperature sensing data. Sensors, 11, 10859-10879.

Huang, N., Jiang, Y., Liu, R., Li, B., Sugimoto, S., 2019. A novel three-dimensional discrete fracture network model for investigating the role of aperture heterogeneity on fluid flow through fractured rock masses. International Journal of Rock Mechanics and Mining Sciences 116, 25-37.

Kneafsey, T.J., Blankenship, D., Dobson, P.F., Morris, J.P., White, M.D., Fu, P. et al., 2020. The EGS Collab Project: Learning from Experiment 1. 45th Workshop on Geothermal Reservoir Engineering, Stanford University, Stanford, CA.

Luo, J., Zhu, Y., Guo, Q., Tan, L., Zhuang, Y., Liu, M. et al., 2017. Experimental investigation of the hydraulic and heat-transfer properties of artificially fractured granite. Scientific Reports 7, 39882.

Nadimi, S., Forbes, B., Moore, J., Podgorney, R., McLennan, J.D., 2020. Utah FORGE: Hydrogeothermal modeling of a granitic based discrete fracture network. Geothermics 87, 101853.

Neupane, G., Mattson, E.D., Plummer, M.A., Podgorney, R.K., EGS Collab Team, 2020. Results of Multiple Tracer Injections into Fractures in the EGS Collab Testbed-1. 45th Workshop on Geothermal Reservoir Engineering, Stanford University, Stanford, CA.

Oldenburg, C.M., Dobson, P.F., Wu, Y., Cook, P.J., Kneafsey, T.J., Nakagawa, S., et al., 2017. Overview of the kISMET project on intermediate-scale hydraulic fracturing in a deep mine. 51st U.S. Rock Mechanics/Geomechanics Symposium, San Francisco, CA.

Patterson, J.W., Driesner, T., 2020. The effect of thermo-elastic stress re-distribution on geothermal production from a vertical fracture zone. Geothermics 85, 101745.

Schwering, P.C., Doe, T.W., Roggenthen, W.M., Neupane, G.H., Johnson, H., Dobson, P.F., Ulrich, C., Singh, A., Uzunlar, N., Reimers, C., 2020. Deterministic Discrete Fracture Network (DFN) Model for the EGS Collab Project on the 4850 Level of the Sanford Underground Research Facility (SURF). 54th U.S. Rock Mechanics/Geomechanics Symposium, Golden, Colorado.

Settgast, R.R., Fu, P., Walsh, S.D.C., White, J.A., Annavarapu, C., Ryerson, F. J., 2017. A fully coupled method for massively parallel simulation of hydraulically driven fractures in 3-dimensions. International Journal for Numerical and Analytical Methods in Geomechanics 41, 627-653.

Shu, B., Zhu, R., Elsworth, D., Dick, J., Liu, S., Tan, J., Zhang, S., 2020. Effect of temperature and confining pressure on the evolution of hydraulic and heat transfer properties of geothermal fracture in granite. Applied Energy 272, 115290.

Tenma, N., Yamaguchi, T., Zyvoloski, G., 2008. The Hijiori Hot Dry Rock test site, Japan. Evaluation and optimization of heat extraction from a two-layered reservoir. Geothermics 37, 19-52.

Tester, J.W., Anderson, B., Batchelor, A., Blackwell, D., DiPippo, R., Drake, E. et al., 2006. The future of geothermal energy: impact of Enhanced Geothermal Systems (EGS) on the United States in the 21st Century. In: Final report to the US Department of Energy Geothermal Technologies Program.

Ulrich, C., Dobson, P.F., Kneafsey, T.J., Roggenthen, W.M., Uzunlar, N., Doe, T.W., et al., 2018. The Distribution, orientation, and characteristics of natural fractures for Experiment 1 of the EGS Collab Project. 52nd U.S. Rock Mechanics/Geomechanics Symposium, Seattle, Washington.

Vik, H.S., Salimzadeh, S., Nick, H.M., 2018. Heat recovery from multiple-fracture enhanced geothermal systems: The effect of thermoelastic fracture interactions. Renewable Energy 121, 606-622.

Wang, Y., Li, T., Chen, Y., Ma, G., 2019. A three-dimensional thermo-hydro-mechanical coupled model for enhanced geothermal systems (EGS) embedded with discrete fracture networks. Computer Methods in Applied Mechanics and Engineering 356, 465-489.

White, M.D., Fu, P., Ghassemi, A., Huang, H., Rutqvist, J., Johnston, B., EGS Collab Team, 2018. Numerical simulation applications in the design of EGS Collab Experiment 1. 43rd Workshop on Geothermal Reservoir Engineering, Stanford University, Stanford, CA.

White, M., Johnson, T., Kneafsey T., Blankenship, D., Fu, P., Wu, H. et al., 2019. The Necessity for Iteration in the Application of Numerical Simulation to EGS: Examples from the EGS Collab Test Bed 1. 44th Workshop on Geothermal Reservoir Engineering, Stanford University, Stanford, CA.

White, M.D., Fu, P., EGS Collab Team., 2020. Application of an embedded fracture and borehole modeling approach to the understanding of EGS Collab Experiment 1. 45th Workshop on Geothermal Reservoir Engineering, Stanford University, Stanford, CA.

Wu, H., Fu, P., Morris, J.P., 2020. Predicting thermal responses at the EGS Collab testbed based on tracer test-inferred flow fields. 45th Workshop on Geothermal Reservoir Engineering, Stanford University, Stanford, CA.

Wu, H., Fu, P., Morris, J.P., Mattson, E.D., Neupane, G., Smith, M.M. et al., 2021. Characterization of flow and transport in a fracture network at the EGS Collab field experiment through stochastic modeling of tracer recovery. Journal of Hydrology 593, 125888.

Xia, Y., Plummer, M., Mattson, E., Podgorney, R., Ghassemi, A., 2017. Design, modeling, and evaluation of a doublet heat extraction model in enhanced geothermal systems. Renewable Energy 105, 232-247.

Xu, T., Yuan, Y., Jia, X., Lei, Y., Li, S., Feng, B. et al., 2018. Prospects of power generation from an enhanced geothermal system by water circulation through two horizontal wells: A case study in the Gonghe Basin, Qinghai Province, China. Energy 148, 196-207.

Zeng, Y., Wu, N., Su, Z., Wang, X., Hu, J., 2013. Numerical simulation of heat production potential from hot dry rock by water circulating through a novel single vertical fracture at Desert Peak geothermal field. Energy 63, 268-282.

Zhang, Y., Dekas, A.E., Hawkins, A.J., Parada, A.E., Gorbatenko, O., Li, K., Horne, R.N., 2020. Microbial community composition in deep-subsurface reservoir fluids reveals natural interwell connectivity. Water Resources Research 56, e2019WR025916.

Zhang, Y., Doughty, C., Pan, L., Kneafsey, T., 2018. What could we see at the production well before the thermal breakthrough? 43rd Workshop on Geothermal Reservoir Engineering, Stanford University, Stanford, CA.